Electromagnetic Modeling of Extended Targets in a Distributed Antenna System

Baptiste Sambon, *Member, IEEE*, François De Saint Moulin, *Student Member, IEEE*, Guillaume Thiran, *Member, IEEE*, Claude Oestges, *Fellow, IEEE*, and Luc Vandendorpe, *Fellow, IEEE*

***Abstract*—Traditional radar and integrated sensing and communication (ISAC) systems often approximate targets as point sources, a simplification that fails to capture the essential scattering characteristics for many applications. This article presents a novel electromagnetic (EM)-based framework to accurately model the near-field (NF) scattering response of extended targets, which is then applied to three canonical shapes: a flat rectangular plate, a sphere, and a cylinder. Mathematical expressions for the received signal are provided in each case. Based on this model, the influence of bandwidth, carrier frequency, and target distance on localization accuracy is analyzed, showing how higher bandwidths and carrier frequencies improve resolution. Additionally, the impact of target curvature on localization performance is studied. Results indicate that detection performance is slightly enhanced when considering curved objects. A comparative analysis between the extended and point-target models shows significant similarities when targets are small and curved. However, as the target size increases or becomes flatter, the point-target model introduces estimation errors owing to model mismatch. The impact of this model mismatch as a function of system parameters is analyzed, and the operational zones where the point abstraction remains valid and where it breaks down are identified. These findings provide theoretical support for experimental results based on point-target models in previous studies.**

***Index Terms*—Electromagnetism, extended target, integrated sensing and communication (ISAC), model mismatch, multistatic, near field (NF), point target, radar, sensing.**

I. Introduction

Sixth-generation (6G) systems are expected to integrate localization and sensing (L&S) with communications to form integrated sensing and communications (ISAC) systems [1]. In this context, sensing performance can be improved by larger bandwidths at higher carrier frequencies and the use of extremely large antenna arrays (ELAAs) [2]. As the frequency and antenna array dimensions increase, the Fraunhofer distance, i.e., the far-field (FF) limit, proportional to the square of the array size and the carrier frequency, grows, expanding the near-field (NF) region.

Most work in radar and ISAC abstracts the target as a single point, which is not valid in the NF region as the target appears spatially extended [3], [4], [5]. This simplified point-target representation is inadequate for various scenarios involving vehicular technologies, such as autonomous driving and guidance radars, as well as high-resolution imaging [6]. In these scenarios, the radar operates in close proximity to the target. This representation also breaks down in situations involving large or spatially extended targets, such as oil tankers, small islands, or large aircraft, where the physical dimensions of the target cannot be ignored [7]. As an example, the experimental results in [8] highlight the impact of multiple backscattering points at mmWave frequencies, emphasizing the need for models that accurately capture extended target responses in the NF. Unfortunately, to the best of the authors' knowledge, a quantitative characterization of the conditions under which a point-target model is sufficient or an extended target model becomes necessary is still lacking.

In the NF region, the spherical nature of the wavefront must be taken into account, adding complexity due to the varying channel gain across antennas. However, this NF effect may offer new possibilities, i.e., by allowing spatial localization rather than just angular estimation [9]. By exploiting NF propagation, both numerical and experimental studies [10], [11] have demonstrated improved localization accuracy. However, the target models used in these studies are restricted to point targets, which limits their ability to capture the full scattering characteristics of extended objects and may lead to biased estimates due to model mismatch.

Several studies in the literature have dealt with extended targets. Part of these works focus on experimental measurements [8] or relies on software simulation tools [12], [13], [14]—for instance, to analyze scattering from physical structures such as buildings [8], to support filter design [12], or to address imaging scenarios [13]. Other works recognize the presence of multiple scattering points but do not model the scattering response of a given specific target [4], [5], [6], [7], [15], [16], [17], [18]. For example, extended target characteristics are handled through clustering points in range–Doppler maps [15] or through-wall radar images [16]. A possible emerging alternative involves point-cloud models, where the target is represented as a collection of discrete points [19]. Compared with these models—which leave open questions regarding the required number and positions of scattering points—we aim here to develop a more abstract and robust framework for characterizing the target response.

Received 28 April 2025; revised 12 August 2025; accepted 23 August 2025. Date of publication 4 September 2025; date of current version 16 September 2025. *(Corresponding author: Baptiste Sambon.)*

Baptiste Sambon, François De Saint Moulin, and Guillaume Thiran are with ICTEAM, UCLouvain, 1348 Louvain-la-Neuve, Belgium, and also with the Fonds de la Recherche Scientifique (FNRS), 1000 Brussels, Belgium (e-mail: baptiste.sambon@uclouvain.be).

Claude Oestges and Luc Vandendorpe are with ICTEAM, UCLouvain, Leuven-la-Neuve, Belgium.

Digital Object Identifier 10.1109/TRS.2025.3605951

In [20], a new NF electromagnetic (EM)-based model is proposed for a flat rectangular plate, which is then used to derive a maximum likelihood (ML) estimator for range. The model is based on the well-known stationary phase approximation (SPA) [21] and provides a closed-form expression for the received signal. By using both amplitude and phase information, the ML estimator shows improved performance compared to traditional range estimators. In addition, performance bounds for this model are derived in [22], showing a degradation in performance when the flat plate is approximated as a single point. However, the scope of the studies presented in these articles is limited; only a flat rectangular plate is considered as the target, with the antenna array constrained to be centered and oriented parallel to the plate surface.

Therefore, this article introduces a general framework for modeling extended targets in the NF, aiming to enhance radar performance, support ISAC channel modeling, and guide beamforming design by accurately characterizing the target response. The validity of the point-target approximation is also assessed, which could enable optimization of the antenna positions (e.g., for minimizing model mismatch and maximizing localization performance).

A. Contributions

Based on the aforementioned works, the contributions of this article are summarized as follows.

1) By leveraging EM theory in conjunction with the well-established SPA, the NF EM-based model of [20] is first generalized to allow for arbitrary target geometries and antenna positions in a multistatic scenario, providing a general closed-form expression for the received signal in the case of extended targets. The model is particularized to three canonical shapes: a flat rectangular plate, a spherical target, and a cylindrical target.
2) Based on this generalized model, numerical analyses are performed for the estimation of the distance between an antenna array and the target, for the three considered target geometries. Namely, they show that similar resolutions are obtained for curved and flat geometries, but lower sidelobe levels are observed in the ambiguity function for curved targets.
3) A stationary point analysis is also performed, highlighting variations in the density of stationary points based on the curvature of the object. This analysis provides insight into the limitations of the point-target approximation.
4) A novel range estimator is developed to perform a model mismatch analysis where the target, though extended, is approximated as a single point. In particular, this analysis derives the range bias introduced by the point-target approximation as a function of system parameters, enabling the identification of operational zones where the point-target approximation remains valid and where it fails. This underscores the necessity for an extended target model in those cases.

B. Structure of This Article

This article is structured as follows. First, the general NF EM-based model is presented in Section II. Then, the SPA used to obtain closed-form expressions is introduced in Section III, followed by its application to a flat rectangular target in Section IV, and to curved targets in Section V. In Section VI, numerical analyses are performed for the estimation of the distance for the three canonical targets and the impact of curvature is analyzed. The impact of the model mismatch on range estimation and a stationary point analysis are presented in Section VII, while a detailed characterization of the mismatch as a function of system parameters is provided in Section VIII.

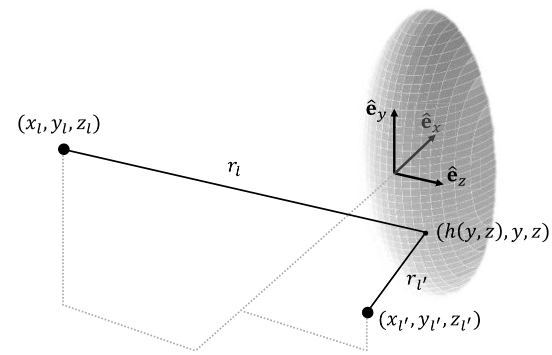

Fig. 1. Reflection on a target between two antennas.

II. Electromagnetic-Based Sensing

The multistatic scenario illustrated in Fig. 1 is considered. The target $\mathcal{S}$ reflects the signals transmitted by a set of N antennas defined as

$$\mathcal{A} \triangleq \left\{(x_l, y_l, z_l) \in \mathbb{R}^3, l = 0, \ldots, N-1\right\}. \tag{1}$$

The shape of the target is modeled through an arbitrary function $h : \mathbb{R} \times \mathbb{R} \to \mathbb{R}$ such that

$$\mathcal{S} \triangleq \left\{(x, y, z) \in \mathbb{R}^3 \middle| x = h(y, z)\right\}. \tag{2}$$

It is also assumed that the function h varies slowly with respect to the wavelength. Thus, the distance r_l from the lth antenna to any point $(x, y, z) \in \mathcal{S}$ is computed as

$$r_l = \sqrt{(h(y,z) - x_l)^2 + (y - y_l)^2 + (z - z_l)^2}. \tag{3}$$

Moreover, the normal unit vector pointing outside the target at the point $(x, y, z) \in \mathcal{S}$ is given by

$$\hat{\mathbf{e}}_n = \frac{-\hat{\mathbf{e}}_x + \frac{\partial h}{\partial y}\hat{\mathbf{e}}_y + \frac{\partial h}{\partial z}\hat{\mathbf{e}}_z}{\sqrt{1 + \left(\frac{\partial h}{\partial y}\right)^2 + \left(\frac{\partial h}{\partial z}\right)^2}}. \tag{4}$$

One can also define the spherical coordinate system associated with the lth antenna as

$$\begin{bmatrix} \hat{\mathbf{e}}_{r_l} \\ \hat{\mathbf{e}}_{\theta_l} \\ \hat{\mathbf{e}}_{\phi_l} \end{bmatrix} \triangleq \begin{bmatrix} \cos\theta_l \cos\phi_l & \sin\theta_l & \cos\theta_l \sin\phi_l \\ -\sin\theta_l \cos\phi_l & \cos\theta_l & -\sin\theta_l \sin\phi_l \\ -\sin\phi_l & 0 & \cos\phi_l \end{bmatrix} \begin{bmatrix} \hat{\mathbf{e}}_x \\ \hat{\mathbf{e}}_y \\ \hat{\mathbf{e}}_z \end{bmatrix} \tag{5}$$

where θ_l and ϕ_l are the elevation and azimuth angles, respectively. The elevation angle is computed from the horizontal plane and the azimuth angle from the x-axis. These angles can be computed for any point $(x, y, z) \in \mathcal{S}$ from the following equalities:

$$\sin\phi_l = \frac{z - z_l}{\sqrt{r_l^2 - (y - y_l)^2}}, \quad \sin\theta_l = \frac{y - y_l}{r_l}$$
$$\cos\phi_l = \frac{h(y, z) - x_l}{\sqrt{r_l^2 - (y - y_l)^2}}, \quad \cos\theta_l = \frac{\sqrt{r_l^2 - (y - y_l)^2}}{r_l}. \quad (6)$$

Assuming that the antennas can be modeled as linear antennas axed along $\hat{\mathbf{e}}_y$, the incident fields from the lth antenna at the point $(x, y, z) \in \mathcal{S}$ of the target are computed as [23]

$$\mathbf{E}_l^i(t) = -jk\eta L I_0 s_l\left(t - \frac{r_l}{c}\right) f(\theta_l) \frac{e^{-jkr_l}}{4\pi r_l} \hat{\mathbf{e}}_{\theta_l}$$
$$\mathbf{H}_l^i(t) = \frac{1}{\eta} \hat{\mathbf{e}}_{r_l} \times \mathbf{E}_l^i(t) \quad (7)$$

with $k = 2\pi/\lambda$ the wavenumber; λ the wavelength; η the free-space impedance; L the antenna length; I_0 the current in the antenna; s_l the signal transmitted by the lth antenna, which can be a communication, radar, or ISAC signal; c the speed of light; and $f(\theta_l)$ the normalized radiation pattern of the antenna. The transmit signal is assumed to have a bandwidth $B \ll c/\lambda$, which is consistent with the quasi-monochromatic assumption, thus enabling this complex time-domain expression [23]. Equation (7) is valid for $r_l \gg \lambda$, which is usually always the case at the considered carrier frequencies, e.g., for automotive radar systems.

Following the physical optics approximation [24], assuming that the target is a good electrical conductor (which is well approximated by a perfect electrical conductor), the equivalent surface current density generated by the lth antenna at the surface of the target is computed from the incident magnetic field as:

$$\mathbf{J}_l(t) = 2\hat{\mathbf{e}}_n \times \mathbf{H}_l^i(t)$$
$$= -2jkLI_0 s_l\left(t - \frac{r_l}{c}\right) f(\theta_l) \frac{e^{-jkr_l}}{4\pi r_l} \left(\hat{\mathbf{e}}_n \times \hat{\mathbf{e}}_{\phi_l}\right). \quad (8)$$

The noise-free received signal at the l'th antenna from the lth antenna is then computed from the equivalent surface current density as [23]

$$u_{l'l}(t) = -jk\eta \iint_{\mathcal{S}} \left(\mathbf{J}_{l'l}^{\perp}\left(t - \frac{r_{l'}}{c}\right) \cdot \mathbf{f}_{l'}^{\perp}\right) \frac{e^{-jkr_{l'}}}{4\pi r_{l'}} d\mathcal{S} \quad (9)$$

where $\mathbf{J}_{l'l}^{\perp}(t) \triangleq \mathbf{J}_l(t) - (\mathbf{J}_l(t) \cdot \hat{\mathbf{e}}_{r_{l'}})\hat{\mathbf{e}}_{r_{l'}}$ is the component of the equivalent surface current density perpendicular to the direction of propagation and $\mathbf{f}_{l'}^{\perp} \triangleq Lf(\theta_{l'})\hat{\mathbf{e}}_{\theta_{l'}}$ is the antenna effective length. In order to simplify (9), one may notice that $\hat{\mathbf{e}}_{r_{l'}} \cdot \hat{\mathbf{e}}_{\theta_{l'}} = 0$ and that $(\hat{\mathbf{e}}_n \times \hat{\mathbf{e}}_{\phi_l}) \cdot \hat{\mathbf{e}}_{\theta_{l'}} = \hat{\mathbf{e}}_n \cdot (\hat{\mathbf{e}}_{\phi_l} \times \hat{\mathbf{e}}_{\theta_{l'}})$, leading to

$$u_{l'l}(t) = -\frac{k^2\eta L^2 I_0}{8\pi^2} \iint_{\mathcal{S}} g_{l'l}(y, z) e^{j\psi_{l'l}(y,z)} d\mathcal{S} \quad (10)$$

where the amplitude function $g_{l'l}$ and the phase function $\psi_{l'l}$ are, respectively, defined as

$$g_{l'l}(y, z) \triangleq s_l\left(t - \frac{r_l + r_{l'}}{c}\right) \frac{f(\theta_l) f(\theta_{l'})}{r_l r_{l'}} \left[\hat{\mathbf{e}}_n \cdot \left(\hat{\mathbf{e}}_{\phi_l} \times \hat{\mathbf{e}}_{\theta_{l'}}\right)\right] \quad (11)$$

$$\psi_{l'l}(y, z) \triangleq -k(r_l + r_{l'}). \quad (12)$$

Equation (10) allows to derive the expression for the received signal for an antenna pair $l'l$ parameterized by the extended target surface function h.

III. Stationary Phase Approximation

The SPA is a powerful tool for approximating integrals of oscillatory functions. It is used here to further develop (10). For univariate integrations, the SPA method is described in [20]. The extension to multivariate integrations is recalled here for the sake of completeness and clarity.

A. Multivariate Integration

The SPA can also be extended to multivariate integrals of the form

$$I = \int_{\Omega} \mathbf{g}(\mathbf{x}) e^{j\psi(\mathbf{x})} d\mathbf{x} \quad (13)$$

where $\mathbf{x} \in \Omega \subseteq \mathbb{R}^n$. The functions $\mathbf{g}$ and ψ are, respectively, named amplitude and phase functions. The stationary point $\mathbf{x}_s$ is still obtained by nullifying the gradient of the phase function, i.e.,

$$\nabla\psi(\mathbf{x})|_{\mathbf{x}=\mathbf{x}_s} = 0. \quad (14)$$

Then, assuming that the amplitude function varies slowly in the vicinity of the stationary point and that the integration domain is large enough to contain multiple oscillations of the phase function, following the same development as in the univariate case, the integral is approximated by:

$$I \approx \mathbf{g}(\mathbf{x}_s) e^{j\psi(\mathbf{x}_s)} (2\pi)^{\frac{n}{2}} \left|\det\left\{\nabla^2\psi(\mathbf{x}_s)\right\}\right|^{-\frac{1}{2}} e^{j\frac{\pi}{4}\mathrm{sgn}\{\nabla^2\psi(\mathbf{x}_s)\}} \quad (15)$$

where $\det\{\cdot\}$ and $\mathrm{sgn}\{\cdot\}$ are, respectively, the determinant and the signature of the Hessian matrix of the phase function. In that case, since the Hessian matrix is symmetric, the signature is either n if the stationary point is a minimum or 0 if it is a saddle point. It should be noted that if there are multiple stationary points, the integral is again approximated by the sum of the contributions of the amplitude function around each stationary point.

In this article, we assume that both assumptions required to apply the SPA are fulfilled. Yet, if the integration domain is not large enough to contain multiple oscillations of the phase function, the last approximation does not hold. In that case, the integration of the phase function may be performed using the Fresnel function [25].

B. Computation of the Stationary Point

For each transmit–receive antenna pair, the received signal is associated with a distinct stationary point on the target surface, depending on the surface function h. This stationary point, denoted as $\mathbf{x}_s = (x_s, y_s, z_s)$, may be located by solving the system of equations provided by (14). Based on the phase function defined as (12), the stationary point should satisfy the following system of equations:

$$\begin{cases} \left.\dfrac{\partial\psi_{l'l}}{\partial y}\right|_{\substack{y=y_s \\ z=z_s}} = 0 \\ \left.\dfrac{\partial\psi_{l'l}}{\partial z}\right|_{\substack{y=y_s \\ z=z_s}} = 0. \end{cases} \quad (16)$$

Let us drop the indices $l'l$ of the phase function and specular points associated with each pair of antennas for the sake of readability. Denoting

$$h_s \equiv h(y_s, z_s) = x_s \tag{17}$$

$$h'_{ys} \equiv \left.\frac{dh}{dy}\right|_{\substack{y=y_s\\z=z_s}}, \quad h'_{zs} \equiv \left.\frac{dh}{dz}\right|_{\substack{y=y_s\\z=z_s}} \tag{18}$$

and

$$r_{ls} \equiv \sqrt{(h_s - x_l)^2 + (y_s - y_l)^2 + (z_s - z_l)^2} \tag{19}$$

the different quantities evaluated at the stationary point, one can show that (16) is developed as follows:

$$\begin{cases} \dfrac{(h_s - x_l)\, h'_{ys} + (y_s - y_l)}{r_{ls}} + \dfrac{(h_s - x_{l'})\, h'_{ys} + (y_s - y_{l'})}{r_{l's}} = 0 \\ \dfrac{(h_s - x_l)\, h'_{zs} + (z_s - z_l)}{r_{ls}} + \dfrac{(h_s - x_{l'})\, h'_{zs} + (z_s - z_{l'})}{r_{l's}} = 0. \end{cases} \tag{20}$$

Note that different coordinate systems may be considered for each pair of antennas and chosen such that $h_s = 0$ and/or $h'_{ys} = h'_{zs} = 0$. In that case, this system of equations can be further simplified. Nonetheless, for many target and antenna geometries, it is difficult to solve these equations analytically. Fortunately, following the Fermat stationary point theorem [26], the stationary point minimizes the total traveled distance $r_l + r_{l'}$. Additionally, the stationary point can also be computed knowing that it corresponds to the specular reflection point, i.e., the point for which the angle of incidence and reflection on the plane are equal.

C. Computation of the Hessian Matrix

Based on the phase function defined as (12), the Hessian matrix can be computed from the first and second derivatives of the function h. For the sake of readability, the indices $l'l$ of the phase function and the specular points associated with each pair of antennas are omitted again. Denoting

$$h''_{ys} \equiv \left.\frac{d^2h}{dy^2}\right|_{\substack{y=y_s\\z=z_s}}, \quad h''_{zs} \equiv \left.\frac{d^2h}{dz^2}\right|_{\substack{y=y_s\\z=z_s}}, \quad h''_{yzs} \equiv \left.\frac{d^2h}{dydz}\right|_{\substack{y=y_s\\z=z_s}} \tag{21}$$

the different quantities evaluated at the stationary point, one can show that the Hessian matrix of the phase function is computed as

$$\nabla^2\psi(\mathbf{x}_s) = \begin{bmatrix} \left.\dfrac{\partial^2\psi}{\partial y^2}\right|_{\mathbf{x}=\mathbf{x}_s} & \left.\dfrac{\partial^2\psi}{\partial y\partial z}\right|_{\mathbf{x}=\mathbf{x}_s} \\ \left.\dfrac{\partial^2\psi}{\partial y\partial z}\right|_{\mathbf{x}=\mathbf{x}_s} & \left.\dfrac{\partial^2\psi}{\partial z^2}\right|_{\mathbf{x}=\mathbf{x}_s} \end{bmatrix} \tag{22}$$

where the different elements of the matrix are given by the following equations:

$$\begin{aligned} \left.\frac{\partial^2\psi}{\partial y^2}\right|_{\mathbf{x}=\mathbf{x}_s} &= \frac{k}{r_{ls}^3}\left[y_s - y_l + (h_s - x_l)\, h'_{ys}\right]^2 \\ &\quad - \frac{k}{r_{ls}}\left[1 + h'^2_{ys} + (h_s - x_l)\, h''_{ys}\right] \\ &\quad + \frac{k}{r_{l's}^3}\left[y_s - y_{l'} + (h_s - x_{l'})\, h'_{ys}\right]^2 \\ &\quad - \frac{k}{r_{l's}}\left[1 + h'^2_{ys} + (h_s - x_{l'})\, h''_{ys}\right] \end{aligned} \tag{23}$$

$$\begin{aligned} \left.\frac{\partial^2\psi}{\partial z^2}\right|_{\mathbf{x}=\mathbf{x}_s} &= \frac{k}{r_{ls}^3}\left[z_s - z_l + (h_s - x_l)\, h'_{zs}\right]^2 \\ &\quad - \frac{k}{r_{ls}}\left[1 + h'^2_{zs} + (h_s - x_l)\, h''_{zs}\right] \\ &\quad + \frac{k}{r_{l's}^3}\left[z_s - z_{l'} + (h_s - x_{l'})\, h'_{zs}\right]^2 \\ &\quad - \frac{k}{r_{l's}}\left[1 + h'^2_{zs} + (h_s - x_{l'})\, h''_{zs}\right] \end{aligned} \tag{24}$$

$$\begin{aligned} \left.\frac{\partial^2\psi}{\partial y\partial z}\right|_{\mathbf{x}=\mathbf{x}_s} &= \frac{k}{r_{ls}^3}\left[y_s - y_l + (h_s - x_l)\, h'_{ys}\right] \\ &\quad \times \left[z_s - z_l + (h_s - x_l)\, h'_{zs}\right] \\ &\quad - \frac{k}{r_{ls}}\left[h'_{ys}h'_{zs} + (h_s - x_l)\, h''_{yzs}\right] \\ &\quad + \frac{k}{r_{l's}^3}\left[y_s - y_{l'} + (h_s - x_{l'})\, h'_{ys}\right] \\ &\quad \times \left[z_s - z_{l'} + (h_s - x_{l'})\, h'_{zs}\right] \\ &\quad - \frac{k}{r_{l's}}\left[h'_{ys}h'_{zs} + (h_s - x_{l'})\, h''_{yzs}\right]. \end{aligned} \tag{25}$$

Again, note that different coordinate systems may be considered for each pair of antennas and chosen such that $h_s = 0$ and/or $h'_{ys} = h'_{zs} = 0$. In that case, these expressions can be further simplified.

D. Comparison With Point-Cloud Models

This section clarifies the distinction between the point-cloud models reviewed in the introduction and the stationary-point set model developed in this work. In point-cloud approaches, the results are highly dependent on the specific choice of scattering points, raising questions regarding their number, spatial distribution, and selection criteria. Both models can be shown to converge as the number of points in the point-cloud model increases. This is expected since the discrete summation of individual scatterer contributions approaches the continuous integral in (10), and the SPA is also an approximation of this integral. In contrast, our model does not require a common set of scattering points for all antenna pairs. Instead, it assigns a single, well-defined specular point to each transmit–receive pair, with the extended target behavior arising from the variation of this stationary point across pairs. Since each point is determined explicitly as the specular point, the proposed model is inherently more compact and robust since the point-cloud approaches naturally lead to results that depend on the arbitrarily determined cloud configuration.

IV. Application to a Flat Rectangular Target

Let us first consider a flat rectangular plate. While De Saint Moulin et al. [20] focus on an antenna array centered and aligned parallel to the plate, this work extends the analysis to arbitrary antenna positions relative to the plate. Without any loss of generality, the shape function h is defined as $h(y,z) = 0$ such that

$$\mathcal{S} \triangleq \left\{ (x,y,z) \in \mathbb{R}^3 \,\middle|\, \begin{matrix} x = 0 \\ |y| \le \dfrac{D_y}{2}, |z| \le \dfrac{D_z}{2} \end{matrix} \right\} \tag{26}$$

with D_y and D_z the dimension of the plate along the y- and z-axes, respectively. The indices $l'l$ of the phase functions and the specular points associated with each pair of antennas are still dropped here. Although the stationary point may, in general, lie outside the plate, we assume in this work that it is located on the plate, i.e., $\mathbf{x}s \in \mathcal{S}$. Additionally, we assume that all antennas are positioned on the same side of the plate such that $x_l < 0$ or $x_l > 0 : \forall : l = 0, \dots, N-1$. While this assumption is not strictly necessary in practice, it significantly simplifies the following analytical calculations.

A. Computation of the Stationary Point

With this target model, since $\mathbf{x}_s \in \mathcal{S}$ and $h(x, y) = 0 : \forall : (x, y) \in \mathcal{S}$, it follows that $h_s = 0$ and $h'_{ys} = h'_{zs} = 0$. The system of equations given in (20) is thus simplified as

$$\begin{cases} \dfrac{y_s - y_l}{r_{ls}} + \dfrac{y_s - y_{l'}}{r_{l's}} = 0 \\ \dfrac{z_s - z_l}{r_{ls}} + \dfrac{z_s - z_{l'}}{r_{l's}} = 0. \end{cases} \tag{27}$$

Unfortunately, except for specific antenna configurations, the solution of this system of equations is not straightforward. Yet, knowing that the stationary point is also the specular reflection point, for the considered target and antenna positions, the following property should hold:

$$\frac{x_l}{r_{ls}} = \frac{x_{l'}}{r_{l's}} \Leftrightarrow \frac{x_l}{x_{l'}} = \frac{r_{ls}}{r_{l's}} \tag{28}$$

leading to

$$y_s = \frac{y_l x_{l'} + y_{l'} x_l}{x_l + x_{l'}}, \quad z_s = \frac{z_l x_{l'} + z_{l'} x_l}{x_l + x_{l'}}. \tag{29}$$

One can notice that if a planar antenna array parallel to the plate is considered, the stationary point is obtained as the arithmetic mean of the antenna positions on the plane.

B. Computation of the Hessian Matrix

With this target model, since $\mathbf{x}_s \in \mathcal{S}$ and $h(x, y) = 0 : \forall : (x, y) \in \mathcal{S}$, it also follows that $h''_{ys} = h''_{zs} = h''_{yzs} = 0$. Thus, using (29), (19) is rewritten as

$$r_{ls} = \frac{2x_l}{x_l + x_{l'}} \underbrace{\frac{1}{2}\sqrt{(x_l + x_{l'})^2 + (y_l - y_{l'})^2 + (z_l - z_{l'})^2}}_{\equiv r_{l'l}}. \tag{30}$$

Consequently, (23)–(25) are simplified as

$$\left.\frac{\partial^2 \psi}{\partial y^2}\right|_{\mathbf{x}=\mathbf{x}_s} = -\frac{k}{r_{l'l}^3} \frac{(x_l + x_{l'})^2}{8 x_l x_{l'}} \left[(x_l + x_{l'})^2 + (z_l - z_{l'})^2\right] \tag{31}$$

$$\left.\frac{\partial^2 \psi}{\partial z^2}\right|_{\mathbf{x}=\mathbf{x}_s} = -\frac{k}{r_{l'l}^3} \frac{(x_l + x_{l'})^2}{8 x_l x_{l'}} \left[(x_l + x_{l'})^2 + (y_l - y_{l'})^2\right] \tag{32}$$

$$\left.\frac{\partial^2 \psi}{\partial y \partial z}\right|_{\mathbf{x}=\mathbf{x}_s} = \frac{k}{r_{l'l}^3} \frac{(x_l + x_{l'})^2}{8 x_l x_{l'}} (y_l - y_{l'})(z_l - z_{l'}). \tag{33}$$

This is further simplified when a linear antenna array is considered along the z-axis or y-axis. For instance, in the first case, $y_l = 0 : \forall : l = 0, \dots, N-1$, leading to

$$r_{l'l} = \frac{1}{2}\sqrt{(x_l + x_{l'})^2 + (z_l - z_{l'})^2} \tag{34}$$

and

$$\left.\frac{\partial^2 \psi}{\partial y^2}\right|_{\mathbf{x}=\mathbf{x}_s} = -\frac{k}{r_{l'l}} \frac{(x_l + x_{l'})^2}{2 x_l x_{l'}} \tag{35}$$

$$\left.\frac{\partial^2 \psi}{\partial z^2}\right|_{\mathbf{x}=\mathbf{x}_s} = -\frac{k}{r_{l'l}^3} \frac{(x_l + x_{l'})^4}{8 x_l x_{l'}} \tag{36}$$

$$\left.\frac{\partial^2 \psi}{\partial y \partial z}\right|_{\mathbf{x}=\mathbf{x}_s} = 0. \tag{37}$$

Consequently, the determinant is also easily computed as

$$\det\left\{\nabla^2 \psi(\mathbf{x}_s)\right\} = \frac{k^2}{r_{l'l}^4} \frac{(x_l + x_{l'})^6}{16 x_l^2 x_{l'}^2}. \tag{38}$$

Applying the SPA, this leads back to the results obtained in [20], considering that $x_l = x_{l'} = -R$ in this article.

V. Application to Curved Targets

In Section IV, it was shown that the SPA can be used to derive an analytical expression for the scattered field of a flat rectangular target. In this section, this analysis is extended to curved targets, specifically considering cylindrical and circular targets. It is found that the SPA method can also be used to derive analytical expressions for the scattered fields of both curved target types.

A. Application to a Spherical Target

For a sphere, the shape function is defined as

$$h(y, z) = \rho - \sqrt{\rho^2 - y^2 - z^2} \tag{39}$$

where ρ is the radius of the sphere. The surface of the sphere is then defined as

$$\mathcal{S} \triangleq \left\{(x, y, z) \in \mathbb{R}^3 \;\middle|\; \begin{array}{c} x = \rho - \sqrt{\rho^2 - y^2 - z^2} \\ |y| \le \rho, |z| \le \rho \end{array}\right\}. \tag{40}$$

The coordinate system is defined such that $h(0, 0) = 0$.

The gradient of the shape function is given by

$$\nabla h(y, z) = \begin{bmatrix} \dfrac{y}{\sqrt{\rho^2 - y^2 - z^2}} \\ \dfrac{z}{\sqrt{\rho^2 - y^2 - z^2}} \end{bmatrix}. \tag{41}$$

Similar to the flat rectangular target, assuming that the stationary point lies on the surface of the sphere, i.e., $\mathbf{x}_s \in \mathcal{S}$, the stationary points are determined by solving (20). For a spherical target, this system is simplified to

$$\begin{cases} \dfrac{(\rho - x_l) y_s - y_l d_s}{r_{ls}} + \dfrac{(\rho - x_{l'}) y_s - y_{l'} d_s}{r_{l's}} = 0 \\ \dfrac{(\rho - x_l) z_s - z_l d_s}{r_{ls}} + \dfrac{(\rho - x_{l'}) z_s - z_{l'} d_s}{r_{l's}} = 0 \end{cases} \tag{42}$$

where $d_s = (\rho^2 - y_s^2 - z_s^2)^{1/2}$. Since the analytical solution to these equations is difficult to compute, the coordinates of the stationary points can be computed numerically by minimizing the total distance traveled $r_l + r_{l'}$ leveraging Fermat's theorem [26].

The Hessian matrix of the shape function h is computed as

$$\nabla^2 h(y,z) = \begin{bmatrix} \dfrac{\rho^2 - y^2}{\left(\rho^2 - y^2 - z^2\right)^{3/2}} & \dfrac{yz}{\left(\rho^2 - y^2 - z^2\right)^{3/2}} \\ \dfrac{yz}{\left(\rho^2 - y^2 - z^2\right)^{3/2}} & \dfrac{\rho^2 - z^2}{\left(\rho^2 - y^2 - z^2\right)^{3/2}} \end{bmatrix}. \quad (43)$$

Based on these expressions, the SPA defined in (15) can be used to calculate the signal $u_{l'l}$ at the receiving antenna by summing the contributions of the two stationary points.

B. Application to a Cylindrical Target

In the case of a cylindrical target, the surface can be described by

$$\mathcal{S} \triangleq \left\{ (x,y,z) \in \mathbb{R}^3 \,\middle|\, \begin{array}{c} x = \rho - \sqrt{\rho^2 - z^2} \\ |y| \leq \dfrac{L}{2}, |z| \leq \rho \end{array} \right\} \quad (44)$$

where L and ρ are the length and radius of the cylinder, respectively. The coordinate system is chosen so that $h(0,0) = 0$ and the origin is at mid-length.

The lack of curvature in the y-direction results in zero derivatives along that axis, resulting in $h'_{ys} = h''_{ys} = h''_{yzs} = 0$. Meanwhile, the derivative in the z-direction is the same as that derived for the spherical target. Consequently, the stationary points can be calculated as follows:

$$\begin{cases} \dfrac{y_s - y_l}{r_{ls}} + \dfrac{y_s - y_{l'}}{r_{l's}} = 0 \\ \dfrac{(\rho - x_l)\, z_s - z_l d_c}{r_{ls}} + \dfrac{(\rho - x_{l'})\, z_s - z_{l'} d_c}{r_{l's}} = 0 \end{cases} \quad (45)$$

where d_c is here equal to $d_c = (\rho^2 - z_s^2)^{1/2}$. The coordinates of the stationary points can be calculated numerically by using Fermat's theorem of stationary points [26]. To compute the determinant of the Hessian matrix of the phase function $\psi(y,z)$ evaluated at the stationary point, the following expression for the second derivatives in the z-direction must be used:

$$h''_{zs} = \frac{\rho^2}{\left(\rho - z_s^2\right)^{3/2}}. \quad (46)$$

The requisite expressions for the SPA problem can then be employed to evaluate the integral (10), using (15).

VI. Impact of Parameters

This section presents a numerical validation and analysis of the EM model. The signals s_l are assigned to orthogonal resources and have a waveform defined by $s_l(t) = (\sin(\pi B t)/\pi B t)$, where B represents the signal bandwidth. Note that, in general, those signals can be communication signals in the case of ISAC applications.

The antennas are arranged linearly along an axis parallel to the z-axis and positioned at $y = 0$. The positions of the antennas are given by $x_l = -R$ and $z_l = (-((N-1)/2) + l)\Delta$, where Δ is the antenna spacing. From now, it is assumed that the elevation and azimuth angles from the center of the array to the target are both equal to zero. Unless stated otherwise, the scenario parameters are those listed in Table I.

TABLE I
Scenario Parameters

Number of antennas	$N = 13$
Antenna spacing	$\Delta = 0.125\,\mathrm{m}$
Antenna length/current	$L^2 I_0 = 1\,\mathrm{m}^2\,\mathrm{A}$
Signal bandwidth	$B = 100\,\mathrm{MHz}$
Carrier frequency	$f_c = 77\,\mathrm{GHz}$
Target dimensions	$D_y = 0.8\,\mathrm{m}$ $D_z = 1.75\,\mathrm{m}$ $\rho = 1.24\,\mathrm{m}$
Target position	$R = 4\,\mathrm{m}$
Elevation angle	$\theta = 0\,°$
Azimuth angle	$\phi = 0\,°$

The impact of the bandwidth B, carrier frequency f_c, and distance R from the target on the log-ML functions of the range estimator introduced in [20] for the flat rectangular plate is here studied for the cylindrical and spherical targets. The range is here defined as the closest distance from the center of the antenna array to the target surface. The profile function of the estimation problem is analyzed, i.e., the value of the log-ML function is evaluated at range $\tilde{R}$ for a target located at range R, in a noise-free scenario.

As shown in Fig. 2, similar results to those obtained in [20] can be observed with flat and curved targets. Indeed, the closer the target, the narrower the main lobe. Additionally, higher bandwidths and carrier frequencies improve the resolution, here defined as the width of the main lobe at −3 dB. Nonetheless, a significant decrease in the sidelobe level is observed with curved geometries. It becomes less likely to confuse the true maximum with a noise-enhanced secondary maximum, causing the flat geometry to be more prone to precision errors. At low signal-to-noise ratio (SNR), with the flat geometry, owing to the null elevation and azimuth angles and the fact that all specular points lie on the target, many antenna pairs receive identical signals. Compared to curved geometries, this results in redundant information, governed by the relative positions of the transmit and receive antennas.

VII. Extended Versus Point-Target Models

This section investigates the effect of model mismatch between the extended and point-target models on range estimation.

A. Profile Function

Let us first compare the normalized profile functions obtained with the point and extended target models for a spherical target of radius $\rho = 1$ m, as shown in Fig. 3. The simulation parameters are given in Table I, except for the carrier frequency and bandwidth, which are here set to $f_c = 3.5$ GHz and $B = 18$ MHz, respectively, to better highlight the model mismatch. In the point-target model, the target is represented as a single point at the origin with coordinates $(0,0,0)$. For the extended target model, the target is centered at $(\rho,0,0)$ in the curved case and at $(0,0,0)$ in the flat case.

It can be seen that the maximum of the profile function for the point-target model does not correspond to the correct

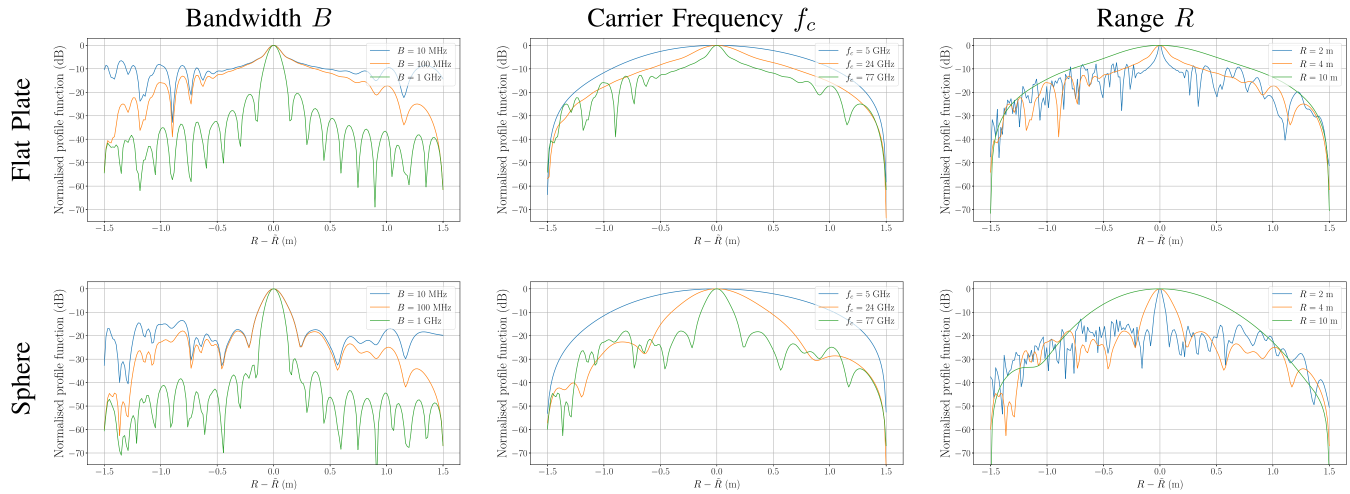

Fig. 2. Impact of the bandwidth B, carrier frequency f_c, and range R on the range profile functions of the two canonical targets.

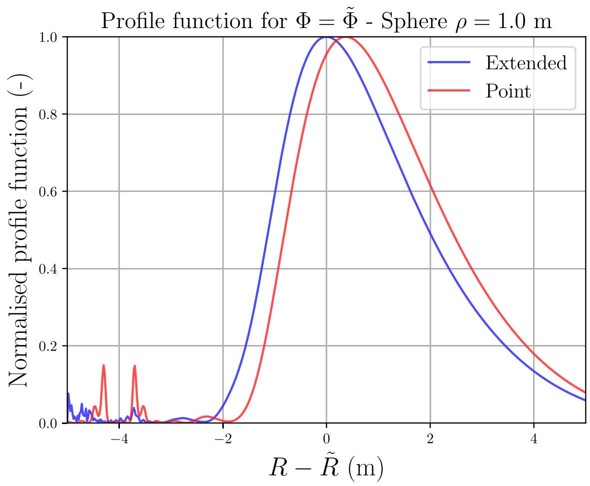

Fig. 3. Profile functions of the extended and point-target models for a spherical target.

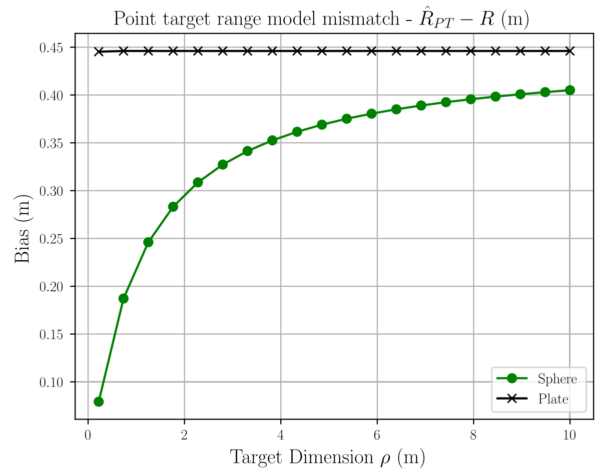

Fig. 4. Point-target model mismatch for increasing dimensions of plate and spherical targets at range $R = 1$ m and antenna spacing $\Delta = \lambda/2 \approx 0.086$ m.

range, whereas this is the case for the extended NF EM model. Therefore, the point-target model does not estimate the correct distance between the center of the antenna array and the target, even in the absence of noise. This is because treating the target as a point causes the model to consider the distances between antennas passing through the center point instead of the specular point for each pair of antennas.

B. Range Model Mismatch

Then, let us compare the mismatch obtained with a sphere and a flat plate while increasing the target dimension. The results are shown in Fig. 4. In this case, ρ denotes the radius of the sphere or half the length for the plate. For example, at a distance $R = 1$ m measured from the center of the antenna array to the closest point on the surface of the target, and antenna spacing $\Delta = \lambda/2 \approx 0.086$ m, when all the stationary points are on the plate—that is, when the plate length is equal to the array size—the distance estimation error for the flat target stabilizes at 0.446 m. This error remains constant as the plate size increases because the stationary points do not shift with larger target sizes. In contrast, the distance estimation error for a sphere increases with its radius, reflecting its increasing similarity to a plate. However, the error for the sphere remains below that of the plate and asymptotically converges to it as the radius of the sphere increases.

C. Stationary Point Analysis

The distribution of the specular points for the three canonical targets, i.e., a flat rectangular target, a sphere, and a cylinder, is analyzed in this section. A 10×10 antenna array with an antenna spacing of 0.1 m to cover the complete target surface, oriented parallel to the yz plane, is positioned at a distance $R = 4$ m from the target. The target has dimensions $L = D_y = D_z = 1$ m and its curvature radius is equal to $\rho = 0.707$ m. Note that the dimensions of the target do not affect the extended model under the SPA.

Fig. 5 shows the spatial distribution of stationary points between each pair of antennas for the three types of targets. The stationary points are relatively evenly distributed over the surface of the flat rectangular target. For the cylindrical

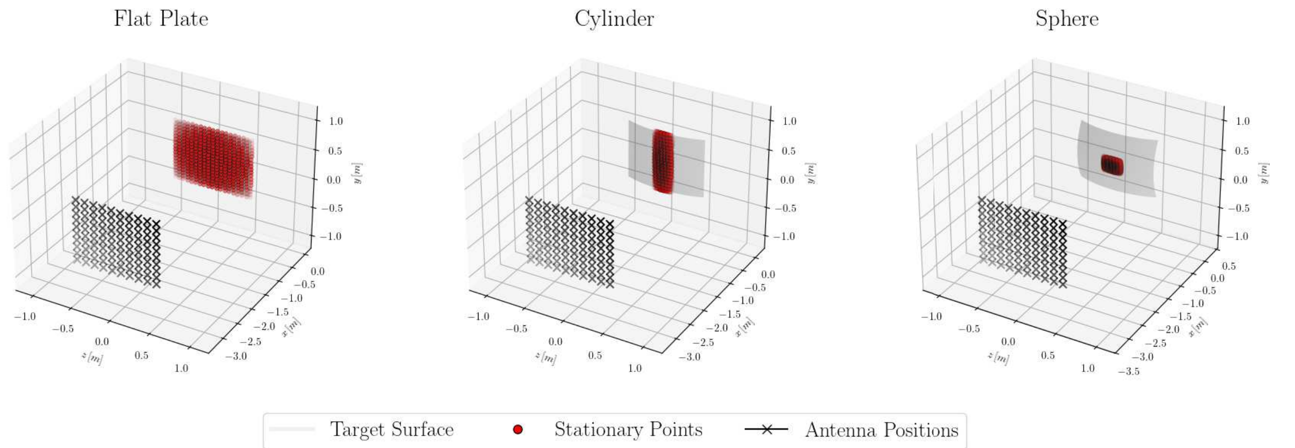

Fig. 5. Analysis of stationary points for the three canonical targets. The antenna positions and specular points locations are, respectively, depicted by black crosses and red dots.

target, despite its 1 m diameter, the stationary points show a higher concentration near the center along the z-axis (axis of curvature) while maintaining a more uniform distribution along the y-axis. In the case of the spherical target, the stationary points are more densely clustered near the point on the sphere closest to the antenna array. With curvature, the stationary points tend to be more concentrated around a single line (resp. point) in the cylinder (resp. sphere) case. This is a consequence of the curvature of the target, which causes the phase to vary more rapidly, resulting in more localized stationary points.

Consequently, the point-target assumption seems to remain reasonable for curved objects, as the stationary points are more concentrated around a single point for curved targets. Yet, this point is not located at the center, but on the surface of the target.

D. Summary

These results show the emergence of a range bias in the profile function of the point-target model for extended targets. This discrepancy results from the assumption for the point-target model that all antenna pairs interact with a single point, rather than accounting for the distributed nature of the target. The observed variation in model mismatch with the target shape can be intuitively explained by the curvature-induced concentration of stationary points.

VIII. Model Mismatch Characterization

This section provides a detailed characterization of the range estimation bias for the point-target model as a function of system parameters.

A. Considered Estimator

In order to evaluate the estimation bias with the point-target model, an alternative range estimator is considered. Compared to the initial estimator proposed in [20], the alternative estimator enables to develop an analytical expression for the bias to be derived, eliminating the need for an exhaustive search of the maximum of the profile function.

This estimator is based on the least-squares error minimization of the total traveled distances between each pair of antennas and can be formulated as

$$\hat{R} = \arg\min_{\tilde{R}} \sum_{l'=0}^{N-1} \sum_{l=0}^{N-1} \left(r_{ls} + r_{l's} - \left(\tilde{r}_{ls;\tilde{R}} + \tilde{r}_{l's;\tilde{R}}\right)\right)^2 \tag{47}$$

where r_{ls} and $r_{l's}$ represent the actual distances to the stationary point for the (l', l) antenna pair, while $\tilde{r}_{ls;\tilde{R}}$ and $\tilde{r}_{l's;\tilde{R}}$ denote their modeled counterparts, which depend on the test range $\tilde{R}$ and the selected model (extended or point target). In the case of a point-target model, the candidate distances no longer depend on the stationary points but on the point chosen to represent the entire target, and could be rewritten as $\tilde{r}_{l;\tilde{R}}$ and $\tilde{r}_{l';\tilde{R}}$.

In practice, the estimation is performed in two steps. First, the total traveled distance $\hat{r}_{ll'} = \hat{r}_l + \hat{r}_{l'}$ is estimated for each antenna pair using the received signals

$$u_{l'l}(t) = A_{l'l} e^{j\psi(\mathbf{x}_{s,l'l})} s_l \left(t - \frac{r_{ls} + r_{l's}}{c}\right) \tag{48}$$

where $A_{ll'}$ is the amplitude factor incorporating the channel effects introduced in Sections II and III. Then, the real distances are replaced by the estimated distance in (47). The problem, as formulated in (47) with the actual traveled distances, therefore represents an idealized scenario and corresponds to a "genie"-aided version. Although this approximation does not hold in practical scenarios, it is still considered here as it allows an analytical expression of the bias to be derived, which facilitates its interpretation and provides bias values that are independent of the specific estimator that would be used to estimate the total traveled distance.

It can be shown that for the same set of parameters, this ideal estimator gives lower biases for the point-target model. This is due to the prior removal of phase-related ambiguities and uncertainties by the use of actual interantenna distances rather than estimated ones, thus providing more accurate range estimates compared to conventional ML approaches. As a result, the model mismatch obtained with this hypothetical estimator serves as a lower bound, meaning that no lower model mismatch can be expected when using the ML estimator described in [20] and used above.

B. Numerical Analyses

This section presents various numerical analyses of the range mismatch, based on the range estimator introduced in Section VIII-A.

1) Linear Antenna Array: First, the analysis of the range mismatch as a function of the system parameters is performed for a linear antenna array.

For a linear array oriented along the z-axis and positioned at $y = 0$, the distance between an antenna at position $\mathbf{x}_l$ and range R, and a point P at position $\mathbf{x}_P$ can be computed using the law of cosines [27], followed by a Taylor series expansion, as

$$\left\|\mathbf{x}_p - \mathbf{x}_l\right\| \approx \tilde{r}_{l;R} + \frac{r_P^2}{2\tilde{r}_{l;R}} - r_P \cos(\phi_l - \phi_P) \tag{49}$$

where ϕ_l and ϕ_P represent the azimuth angles and $\tilde{r}_{l;R}$ and r_P denote the distances from the antenna and point P to the origin of the coordinate system, respectively. Under the per-antenna FF assumption, which is valid when $R \gg r_P$, and assuming that the target representative point is located at $\theta_P = \pi/2$, the estimation of the range for a single point comes to estimating the distance r_P, i.e., $\hat{r}_P = \hat{R}$. Consequently, the range mismatch for all antenna pairs, based on the range estimation defined in (47), can be expressed as

$$\begin{aligned}&\hat{R} - R\\ &= \frac{\sum_{l=0}^{N-1}\sum_{l'=0}^{N-1}\left(\left(\tilde{r}_{l;R} + \tilde{r}_{l';R}\right) - \left(r_{ls} + r_{l's}\right)\right)\left(\sin\theta_l + \sin\theta_{l'}\right)}{\sum_{l'=0}^{N-1}\sum_{l=0}^{N-1}\left(\sin\theta_l + \sin\theta_{l'}\right)^2}.\end{aligned} \tag{50}$$

The mismatch for the point model comes from considering the distances $\tilde{r}_{l;R}$ and $\tilde{r}_{l';R}$ to the single reference point representing the target for all pairs of antennas, rather than using the stationary points. The bias obtained with the point-target model can be seen as a weighted sum of the discrepancies between the actual propagation distances and those to the reference point. It can also be noted that the extended target model does not introduce any bias as it accurately accounts for the distances to the stationary points.

Fig. 6 further investigates the range estimation bias due to model mismatch for a spherical target with this idealistic estimator, leveraging (50). The range bias evolution is shown as a function of the range R, sphere radius ρ, and antenna spacing Δ. The analysis is based on a linear array of 13 antennas. Note that the color scales are not identical across the subfigures. The impact of the system parameters can be described as follows.

1) *Range R:* As the range increases, the mismatch decreases because the spherical target appears more like a single point from the perspective of the antenna array.
2) *Antenna Spacing Δ:* Greater biases are obtained as the distance between the antennas increases, corresponding to a larger array size. This effect occurs because, as the array expands, the discrepancy between the actual distances to the stationary points and those to the representative target point becomes more pronounced since the stationary points move further away from the assumed reference point.
3) *Radius ρ:* As the sphere size decreases, this distance difference diminishes because the stationary points are closer to this abstracting point. However, if the radius of curvature of the sphere increases, the estimation error due to mismatch also increases. In this case, a flatter geometry from the perspective of the antenna array results in an increased mismatch.

In the case of a large antenna array, the expected mismatches can thus become significant, particularly if the target is large and at close range. On the contrary, for a more distant target, with a smaller antenna array or reduced size target, abstracting the target to a single point seems more reasonable.

2) Distributed Antennas: Section VIII-B1 analyzed the range mismatch for a given antenna array. However, the developed EM target model is also applicable to distributed antenna configurations. Therefore, this section extends the mismatch analysis to this scenario.

For this analysis, three 13-element antenna arrays aligned along the z-axis and positioned at $y = 0$ are considered. Within each subarray, the antennas are spaced at $\lambda/2 \approx 0.086$ m, corresponding to a carrier frequency of $f_c = 3.5$ GHz.

Fig. 7 illustrates the relative range mismatch as a function of the subarray spacing. The central subarray is positioned at $z = 0$, facing the target, while the other two subarrays are positioned symmetrically along the z-axis—one shifted in the positive z-direction and the other shifted in the negative direction by a specified subarray spacing measured from center to center. Two types of targets are considered at different ranges R: a spherical target and a flat rectangular plate, each with a radius or half-length of $\rho = 1$ m.

Similar to the single array case, the distributed configuration shows a higher range mismatch for the flat target compared to the curved target for the same set of parameters. As the system becomes more distributed (i.e., as the subarray spacing increases), the relative mismatch becomes more significant. This behavior is attributed to the fact that the stationary points become more dispersed, deviating from the single point approximation. An increase in range leads to a reduction in relative mismatch levels, consistent with the observations and explanations in Section VIII-B1, but here for a distributed scenario.

Therefore, depending on the scenario, the model mismatch can vary significantly, from negligible in cases of curved targets and small arrays at greater distances, to detrimental in scenarios with flatter, closer targets and more distributed antenna configurations. In this context, analyses similar to Figs. 6 and 7 can be used to estimate the minimum expected model mismatch or relative error for a given scenario.

3) Equipotential Curves: Equipotential curves, i.e., curves for which a given set of system parameters gives the same range mismatch, can be obtained by equating (50) to a specified bias value α. Besides, if a certain range mismatch maximum threshold α is defined as acceptable, these curves delineate the limits of the operating region within which the point-target approximation remains valid.

For example, for a given antenna array, assuming that the antenna spacing is small compared to the range, i.e., $R \gg \Delta$, the equipotential curve equation for a given range bias α in

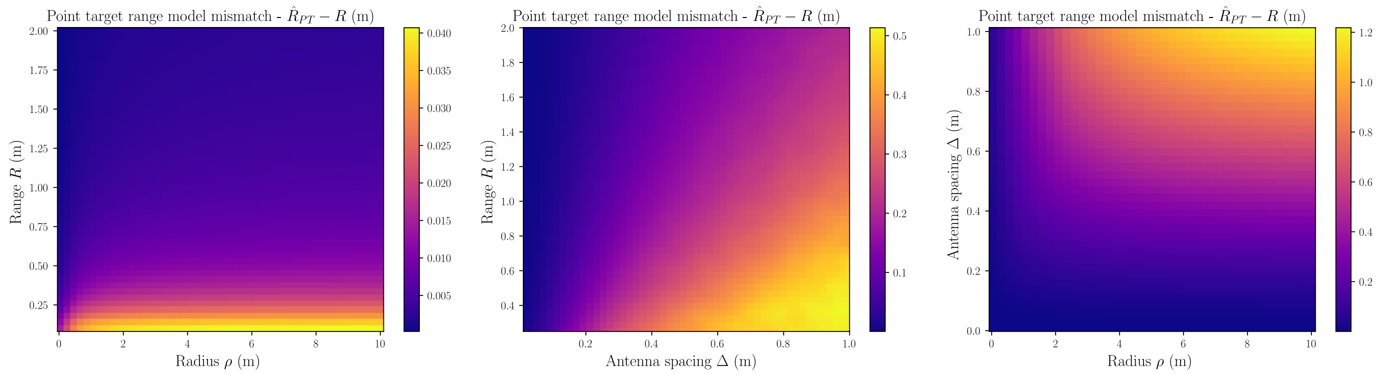

(a) (b) (c)

Fig. 6. Range bias analysis for the point-target model and the spherical target as a function of the sphere radius ρ, the range R, and the antenna spacing Δ using the least-squares error minimization estimator. (a) Range—radius, antenna spacing $\Delta = \lambda/2 \approx 0.086$ m. (b) Range—antenna spacing, radius $\rho = 1$ m. (c) Antenna spacing—radius, range $R = 1$ m.

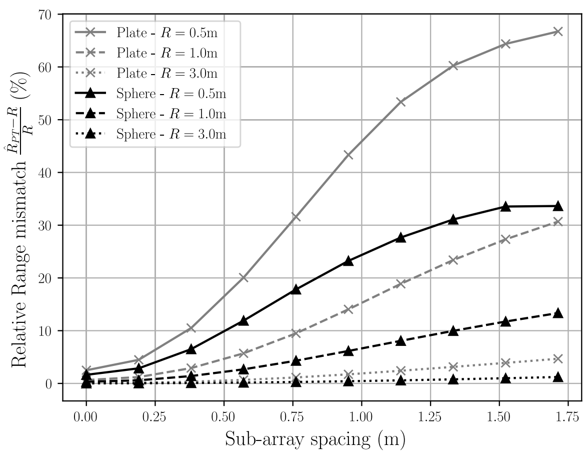

Fig. 7. Relative range mismatch in a distributed antenna array configuration of three 13-antenna arrays as a function of subarray spacing for a spherical target and rectangular plate.

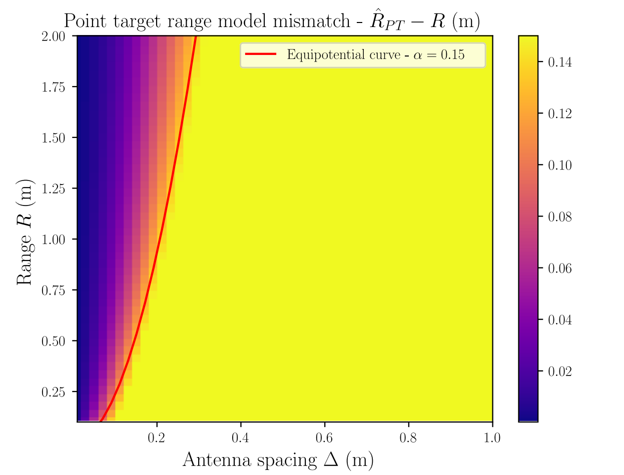

Fig. 8. Equipotential curve for the range mismatch analysis as a function of the range R and antenna spacing Δ for a flat plate.

the case of a flat plate target and a single antenna array is given by

$$R = \frac{\sum_{l'=0}^{N-1}\sum_{l=0}^{N-1}\left(\frac{\left(l-\frac{N-1}{2}\right)^2+\left(l'-\frac{N-1}{2}\right)^2}{2} - \frac{(l-l')^2}{2}\right)}{2\,N^2\alpha}\Delta^2 \qquad (51)$$

where all the stationary points are assumed to be located on the plate.

An illustration of such curve is given in red in Fig. 8 and illustrates the quadratic relation between the range and antenna spacing at constant bias for $\alpha = 0.15$ m. It can be seen that the analytical curve derived from (51) fits well with the thresholded mismatch color map obtained with (50). In this way, (51) can be used to determine the range-antenna spacing parameter pairs $(R;\Delta)$ that give rise to the same bias in the range estimate with a point-target model of a rectangular flat plate. Moreover, if the range mismatch threshold α is predefined as permissible, this curve also delineates the operational zone within which the point-target approximation remains valid. In Fig. 8, this corresponds to the (nonyellow) region at the left of the red curve.

For other target geometries, such as the sphere or cylinder, obtaining an analytical expression for the potential curves is more complicated. In such cases, analyses based on the color maps shown in Fig. 6 can be performed by looking at the zones where the range mismatch is equal to a given value α.

4) Summary: To summarize, Figs. 4–6 show that the point-target approximation performs well when the dimensions of the target are relatively small with respect to the array size, and it exhibits curvature. In this context, the flat target scenario represents a worst case condition for point-target approximation, explaining the limitations raised in [22]. This phenomenon also explains the accurate localization obtained experimentally by Sakhnini et al. [10], [11] when considering a small cylinder as single point. However, for larger target or antenna array dimensions, specular points have a greater tendency to deviate from the single point case and larger model mismatch estimation errors can occur, as illustrated in Figs. 6 and 7. In such cases, the extended target model developed in this work, which takes the spatial distribution of stationary points into account, should be used for an accurate characterization and estimation. To determine the extent to which the point-target assumption remains valid, equipotential curves similar to (51) and Fig. 8 can be used.

IX. Conclusion

This article provides a comprehensive analysis and validation of an EM-based signal model for an arbitrary target in the NF region of an arbitrary network of antennas, based on the SPA method. Further developments are made to provide mathematical solutions for three canonical targets, i.e., flat rectangular plate, sphere, and cylinder. First, the profile function analysis of a range ML estimator showed high accuracy, with target curvature effectively reducing sidelobes. Furthermore, a model mismatch analysis with the point-target model showed an increasing estimation error with increasing array size and radius of curvature, and a stationary point analysis revealed a concentration of stationary points at the center of curved targets. These results highlight the relevancy of point-target models and explain the accurate localization observed in other NF sensing papers, when small curved objects are approximated as point targets [10], [11]. Nonetheless, as soon as the target dimensions become relatively large compared to the antenna array size, this approximation is no longer valid and the extended target model must be taken into account. The operational regions where the point-target assumption holds or fails for a given mismatch value have been derived.

Future work will explore NF communication channel characterization with extended obstacles, estimation of the target shape and sensing of multiple targets, and the study of efficient algorithms for 3-D localization.

References

[1] H. Chen et al., “6G localization and sensing in the near field: Features, opportunities, and challenges,” *IEEE Wireless Commun.*, vol. 31, no. 4, pp. 260–267, Aug. 2024.

[2] S. Ye et al., “Extremely large aperture array (ELAA) communications: Foundations, research advances and challenges,” *IEEE Open J. Commun. Soc.*, vol. 5, pp. 7075–7120, 2024.

[3] R. Liu, A. Lee Swindlehurst, and M. Li, “CRB optimization using a parametric scattering model for extended targets in ISAC systems,” 2024, *arXiv:2411.00145*.

[4] Y. Wang, M. Tao, S. Sun, and W. Cao, “Cramér-rao bound analysis and beamforming design for 3D extended target in ISAC,” in *Proc. IEEE Global Commun. Conf.*, Dec. 2024, pp. 5344–5349.

[5] J. Cong et al., “Near-field integrated sensing and communication: Opportunities and challenges,” *IEEE Wireless Commun.*, vol. 31, no. 6, pp. 162–169, Dec. 2024.

[6] R. Liu, A. L. Swindlehurst, and M. Li, “CRB optimization using a parametric scattering model for extended targets in ISAC systems,” in *Proc. IEEE Int. Radar Conf. (RADAR)*, May 2025, pp. 1–6.

[7] Y. Chen, K. Guo, Z. Liu, and X. Sheng, “Near-field scattering centre modelling for complex targets,” *IET Radar, Sonar Navigat.*, vol. 18, no. 12, pp. 2657–2666, Dec. 2024.

[8] H. Khosravi, X. Cai, and F. Tufvesson, “Experimental analysis of physical interacting objects of a building at mmWave frequencies,” in *Proc. 18th Eur. Conf. Antennas Propag. (EuCAP)*, Mar. 2024, pp. 01–05.

[9] Y. Liu, Z. Wang, J. Xu, C. Ouyang, X. Mu, and R. Schober, “Near-field communications: A tutorial review,” *IEEE Open J. Commun. Soc.*, vol. 4, pp. 1999–2049, 2023.

[10] A. Sakhnini, S. De Bast, M. Guenach, A. Bourdoux, H. Sahli, and S. Pollin, “Near-field coherent radar sensing using a massive MIMO communication testbed,” *IEEE Trans. Wireless Commun.*, vol. 21, no. 8, pp. 6256–6270, Aug. 2022.

[11] A. Sakhnini, S. De Bast, M. Guenach, A. Bourdoux, H. Sahli, and S. Pollin, “An experimental evaluation of robust near-field radar localization using a massive MIMO testbed,” in *Proc. 2nd IEEE Int. Symp. Joint Commun. Sens.*, Mar. 2022, pp. 1–6.

[12] S. M. Karbasi, A. Aubry, A. De Maio, and M. H. Bastani, “Robust transmit code and receive filter design for extended targets in clutter,” *IEEE Trans. Signal Process.*, vol. 63, no. 8, pp. 1965–1976, Apr. 2015.

[13] S. Sruti, A. A. Kumar, and K. Giridhar, “RCS-based imaging of extended targets for classification in multistatic radar systems,” in *Proc. IEEE Radar Conf.*, May 2023, pp. 1–6.

[14] M. M. H. Amir, S. Maresca, G. Serafino, P. Ghelfi, and A. Bogoni, “Modelling of extended targets with dual-band MIMO radar networks,” in *Proc. 18th Eur. Radar Conf. (EuRAD)*, Apr. 2022, pp. 345–348.

[15] F. Pedraza, S. K. Dehkordi, J. C. Hauffen, S. Li, P. Jung, and G. Caire, “Extended target parameter estimation and tracking with an HDA setup for ISAC applications,” in *Proc. IEEE Globecom Workshops*, Dec. 2023, pp. 117–122.

[16] G. Gennarelli, G. Vivone, P. Braca, F. Soldovieri, and M. G. Amin, “Multiple extended target tracking for through-wall radars,” *IEEE Trans. Geosci. Remote Sens.*, vol. 53, no. 12, pp. 6482–6494, Dec. 2015.

[17] Z. Du et al., “Integrated sensing and communications for V2I networks: Dynamic predictive beamforming for extended vehicle targets,” *IEEE Trans. Wireless Commun.*, vol. 22, no. 6, pp. 3612–3627,Jun. 2023.

[18] Z.-J. Wu, C.-X. Wang, Y.-C. Li, and Z.-Q. Zhou, “Extended target estimation and recognition based on multimodel approach and waveform diversity for cognitive radar,” *IEEE Trans. Geosci. Remote Sens.*, vol. 60, 2022, Art. no. 5101014, doi: 10.1109/TGRS.2021.3065335.

[19] P. Koivumäki, G. Steinböck, and K. Haneda, “Impacts of point cloud modeling on the accuracy of ray-based multipath propagation simulations,” *IEEE Trans. Antennas Propag.*, vol. 69, no. 8, pp. 4737–4747, Aug. 2021.

[20] F. De Saint Moulin, G. Thiran, C. Craeye, L. Vandendorpe, and C. Oestges, “Near-field EM-based multistatic radar range estimation,” in *Proc. 32nd Eur. Signal Process. Conf. (EUSIPCO)*, Aug. 2024, pp. 2407–2411.

[21] N. Bleistein and R. Handelsman, *Asymptotic Expansions of Integrals*. New York, NY, USA: Dover, 1975.

[22] G. Thiran, F. De Saint Moulin, C. Oestges, and L. Vandendorpe, “Performance bounds for near-field multi-antenna range estimation of extended targets,” in *Proc. IEEE 25th Int. Workshop Signal Process. Adv. Wireless Commun.*, Sep. 2024, pp. 261–265.

[23] S. J. Orfanidis, *Electromagnetic Waves and Antennas*. New Brunswick, NJ, USA: Rutgers Univ. Press, 2016.

[24] J. Gutierrez-Meana, A. Jose, and F. Las-Heras, “High frequency techniques: The physical optics approximation and the modified equivalent current approximation (MECA),” in *Electromagnetic Waves Propagation in Complex Matter*. London, U.K.: IntechOpen, Jul. 2011.

[25] M. Abramowitz and I. A. Stegun, *Handbook of Mathematical Functions: With Formulas, Graphs, and Mathematical Tables*. Chelmsford, MA, USA: Courier Corp., Jan. 1965.

[26] F. P. Miller, A. F. Vandome, and J. McBrewster, *Fermat's Theorem (Stationary Points): Theorem, Real Analysis, Pierre De Fermat, Maxima and Minima, Derivative, Open Set, Stationary Point, Equation, Necessary and Sufficient Condition, Inflection Point, Second Derivative*. San Carlos, CA, USA: Alphascript, Dec. 2009.

[27] C. A. Pickover, *The Math Book: From Pythagoras to the 57th Dimension, 250 Milestones in the History of Mathematics*. New York, NY, USA: Sterling Publishing Company, 2009.

Baptiste Sambon (Member, IEEE) received the B.Sc. and M.Sc. degrees (summa cum laude) in electrical engineering from Université Catholique de Louvain (UCLouvain), Ottignies-Louvain-la-Neuve, Belgium, in 2022 and 2024, respectively, where he is currently pursuing the Ph.D. degree within the Institute for Information and Communication Technologies, Electronics and Applied Mathematics, (ICTEAM), as a Fonds de la Recherche Scientifique (FNRS) Research Fellow.

His research interests include integrated sensing and communication (ISAC) technologies, near-field target and channel modeling, and signal processing for radar and communication.

François De Saint Moulin (Student Member, IEEE) received the B.Sc. and M.Sc. degrees in electrical engineering from the Université Catholique de Louvain, (UCLouvain), Louvain-la-Neuve, Belgium, in 2018 and 2020, respectively, and the Ph.D. degree from the Institute for Information and Communication Technologies, Electronics and Applied Mathematics, (ICTEAM), UCLouvain, in 2024.

He is a Research Fellow of the Fonds de la Recherche Scientifique (FNRS). His research interests include integrated sensing and communication technologies, near-field channel modeling and signal processing for radar and communication, and stochastic geometry.

Guillaume Thiran (Member, IEEE) received the M.Sc. degree (summa cum laude) in electrical engineering from the Université Catholique de Louvain, Louvain-la-Neuve, Belgium, in 2020, and the Ph.D. degree as an FNRS Research Fellow, Université Catholique de Louvain, in 2024, under the supervision of Prof. L. Vandendorpe.

His general interests span the area of wireless communications, game theory and network coding. His research focuses on competitive resource allocation schemes in MEC networks through multiobjective game theory.

Claude Oestges (Fellow, IEEE) received the M.Sc. and Ph.D. degrees from Université Catholique de Louvain (UCLouvain), Ottignies-Louvain-la-Neuve, Belgium, in 1996 and 2000, respectively.

After a postdoc with Stanford University, he became Full Professor UCLouvain's ICTEAM institute. He has authored four books and more than 200 publications. His research focuses on wireless and satellite communication channels and their effect on system performance.

Dr. Oestges is the past Chair of COST IRACON, and former EurAAP Board Member. He was the recipient of the IET Marconi Award in 2001, IEEE Neal Shepherd Awards in 2004 and 2013, respectively, and the EurAAP Propagation Award in 2024.

Luc Vandendorpe (Fellow, IEEE) was born in Mouscron, Belgium, in 1962. He received the M.Sc. degree (summa cum laude) in electrical engineering and the Ph.D. degree in applied science from the Catholic University of Louvain (UCLouvain), Louvain-la-Neuve, Belgium, in 1985 and 1991, respectively.

He is currently a Full Professor with the Institute for Information and Communication Technologies, Electronics, and Applied Mathematics, UCLouvain. He is investigating wireless systems operating in the near-field (extra-large antenna arrays and cell-free networks) and capable of joint communications and sensing. He is addressing signal processing challenges formalized thanks to the electromagnetic theory. His research interests include digital communication systems and sensing/localization/positioning techniques.

Dr. Vandendorpe is or has been a TPC Member of numerous IEEE conferences, such as VTC, GLOBECOM, SPAWC, ICC, PIMRC, and WCNC. He was an elected member of the Signal Processing for Communications Committee from 2000 to 2005 and an elected member of the Sensor Array and Multichannel Signal Processing Committee of the Signal Processing Society from 2006 to 2008 and from 2009 to 2011. He was the Chair of the IEEE Benelux Joint Chapter on communications and vehicular technology from 1999 to 2003. He was the Co-Technical Chair of IEEE ICASSP 2006. He served as an Editor for Synchronization and Equalization of IEEE TRANSACTIONS ON COMMUNICATIONS from 2000 to 2002. He served as an Associate Editor for IEEE TRANSACTIONS ON WIRELESS COMMUNICATIONS from 2003 to 2005 and IEEE TRANSACTIONS ON SIGNAL PROCESSING from 2004 to 2006.